


SOLPS simulations of detachment in a snowflake configuration for the future upper divertor in ASDEX Upgrade

O Pan^{1,2} , T Lunt¹, M Wischmeier¹, D Coster¹ and the ASDEX Upgrade team

¹Max-Planck-Institut für Plasmaphysik, D-85748 Garching, Germany

²Physik-Department E28, Technische Universität München, D-85747 Garching, Germany

E-mail: ou.pan@ipp.mpg.de

Received 26 March 2018, revised 2 May 2018

Accepted for publication 22 May 2018

Published 13 June 2018



CrossMark

Abstract

We report on the first SOLPS simulations of a low-field side snowflake minus (LFS SF⁻) configuration in ASDEX Upgrade (AUG). This configuration will become accessible in AUG after the foreseen hardware modification of its upper divertor. Spatially constant transport coefficients, an input power of 5 MW and a nitrogen seeding rate leading to a radiative fraction of 86% were assumed. This radiative fraction is 9% higher than that for a single null reference with the same transport coefficients, similar upstream parameters and separatrix impurity concentrations. As a consequence the LFS SF⁻ configuration achieves a larger degree of detachment and reduced heat fluxes to the targets. This heat flux mitigation was found to be significantly stronger than that expected from a simple scrape-off layer splitting model.

Keywords: SOLPS simulation, snowflake divertor, detachment

(Some figures may appear in colour only in the online journal)

1. Introduction

Alternative divertor geometries, such as an x-divertor (XD) [1] or a low-field side snowflake minus (LFS SF⁻) configuration [2] are currently discussed as a possible solution for the power exhaust problem in a fusion reactor. For this reason ASDEX Upgrade (AUG) recently decided the installation of a pair of in-vessel coils to study these configurations experimentally [3] in a machine with a high heating power compared to its size. For the planning of this hardware modification the edge transport code EMC3-EIRENE [4] was used. Due to the possibility to run EMC3-EIRENE on a non-flux-surface aligned grid the implementation of the magnetic field geometry is straight forward, even if its topology differs from the axi-symmetric single null (SN) case [5]. EMC3-EIRENE is also an indispensable tool to

model 3D effects in the scrape-off layer (SOL) transport, such as error fields caused by the current feeds (particularly important for the XD configuration, where very shallow field line angles occur), by intentionally applied 3D fields to control edge-localized modes or for 3D plasma-facing components [6]. However, volumetric recombination and drifts are currently not implemented in the code. These two processes were required to reproduce important features of the experimentally diagnosed AUG SOL plasma in the SN configuration, including the low-field-side/high-field-side asymmetries [7], in recent SOLPS simulations of the detached divertor state [8]. The access to detachment will be an important criterion to evaluate the suitability of the different configurations for a reactor that will need to operate at least partially in that regime. Due to its technical requirement of a block-shaped computational grid, SF topologies could not be simulated with SOLPS so far. This technical requirement was now met by fulfilling different constraints on the grid resolution and mapping the spatial SF grid to the computational grid in an appropriate way. One goal of the study presented in this article is to demonstrate the applicability of



Original content from this work may be used under the terms of the [Creative Commons Attribution 3.0 licence](https://creativecommons.org/licenses/by/3.0/). Any further distribution of this work must maintain attribution to the author(s) and the title of the work, journal citation and DOI.

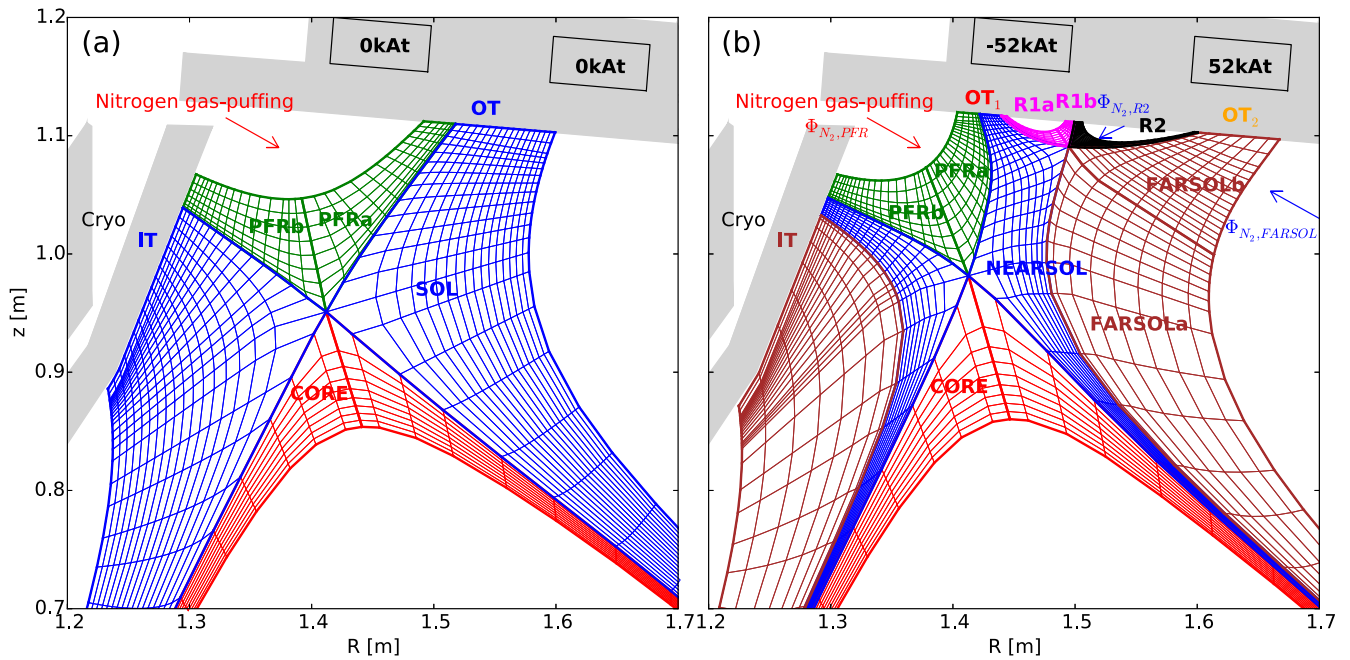


Figure 1. Physical simulation grids of (a) single null (SN) and (b) low-field side snowflake minus (LFS SF⁻) geometries.

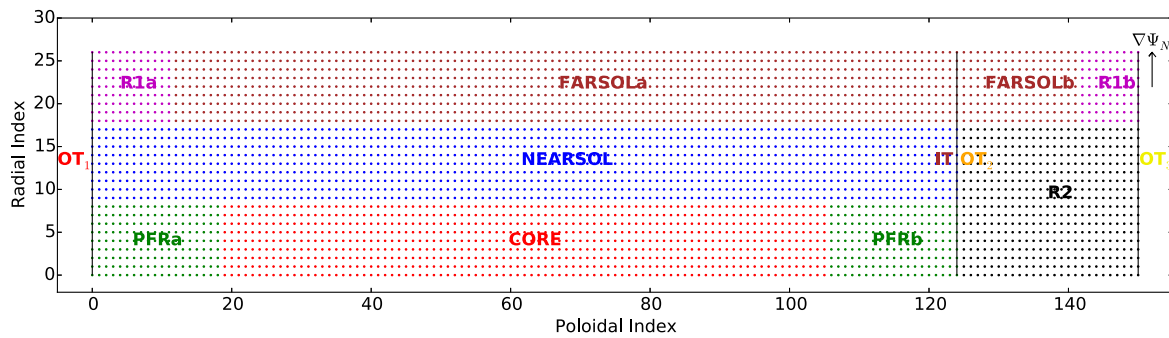


Figure 2. Block-shaped computational grid for the LFS SF⁻ configuration shown in figure 1(b). The vertical lines indicate the inner (IT) and outer targets close to the primary (OT₁) and secondary (OT₂) strike points.

SOLPS to such a topology in general. In addition to that detached divertor conditions will be studied in particular. We report here on the first SOLPS simulations of this type so far. Other two-dimensional multi-fluid codes such as UEDGE and SOLEDGE2D have also been used to model snowflake-like configurations with the secondary X-point near the target in NSTX [9], NSTX-U [10] and HL-2M [11]. These simulations generally found divertor detachment either at a lower density, or at a lower impurity seeding fraction, as compared to the standard divertor, which was attributed to the increased plasma-wetted area and connection length as well as increased radiative power losses. Here we show simulations where the secondary X-point is located much further away from the target poloidally and radially within the first power fall-off length of the SOL.

2. Implementation of the geometry

After the foreseen hardware upgrade, the configurations shown in figure 1 of [3] will be achievable with the future upper

divertor in AUG. In this article we focus on the (upper) SN and the LFS SF⁻ configurations. Here the LFS SF⁻ configuration with a distance $r_{u,x_2} = 1.8$ mm between primary and secondary separatrices at the outboard mid-plane was chosen according to previous EMC3-EIRENE simulations used for the planning of this hardware upgrade [3]. In future experiments, r_{u,x_2} can be adjusted by varying the currents in the in-vessel poloidal field coils. Physical grids for these configurations are shown in figure 1. These grids were not produced using the grid generator tool ‘carre’ which is part of the SOLPS package, but with the one developed for EMC3-EIRENE which was adapted to the requirements of SOLPS. The grid for the LFS SF⁻ case consists of six regions which we refer to as ‘confinement region’ (CORE, red), ‘near SOL’ (NEARSOL, blue), ‘far SOL’ (FARSOL, brown), ‘private flux region’ (PFR, green), and ‘remote areas’ one (R1, magenta) and two (R2, black). The SN configuration only consists of the first three. An important technical constraint is that the physical grid needs to be represented by a block-shaped computational grid, as mentioned in the introduction. This requirement is met by dividing the PFR, FARSOL, and R1

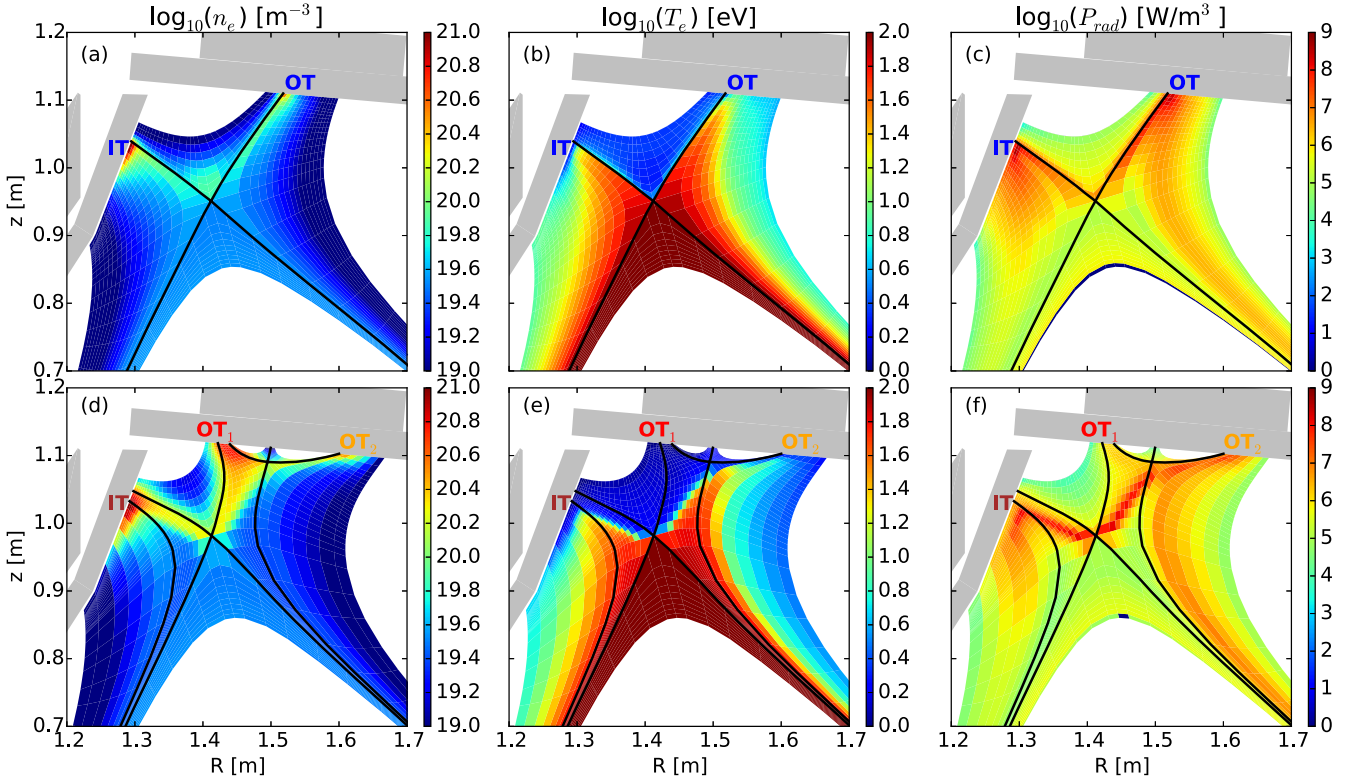


Figure 3. Simulation results of electron density (a), (d), electron temperature (b), (e) and radiation (c), (f) for the high nitrogen seeding case B. The top row (a)–(c) shows the SN and the lower row (d)–(f) the LFS SF^- geometry. The corresponding target profiles are shown in figure 4(b).

regions into two sub-regions each and choosing the radial resolution of the R2 region as large as that of the CORE and NEARSOL together as well as the poloidal resolution of the R2 region as large as that of the FARSOLb and R1b together (see figure 2). The radial resolution of the R1 regions is equal to that of the FARSOL regions. For every poloidal index the normalized poloidal flux Ψ_N is increasing monotonically with increasing radial index. The inner target (IT) as well as the primary (OT₁) and secondary (OT₂) outer ones are also shown in figure 2 as vertical lines.

The plasma and neutral particle transport is simulated by the SOLPS5.0 code package [12], which includes the B2.5 multi-fluid transport code [13] coupled to the EIRENE Monte Carlo code [14]. The transport of electrons and ions of deuterium (D) and nitrogen (N) at each ionization state are handled by B2.5, while the neutral particle transport and the corresponding atomic and molecular processes are modeled by EIRENE. The reactions activated in this simulation include deuterium physics which are essentially the same as those described in [15], as well as the ionization, dissociation and recombination of the seeded nitrogen. The nitrogen-deuterium charge exchange reaction is assumed to be negligible here because of its non-resonant character, while the nitrogen-nitrogen charge exchange is neglected due to the small concentration n_{N^+}/n_{D^+} in the confinement region and SOL. Ions that leave the grid across the last radial grid surface or hit the target as well as neutrals hitting the main chamber wall are fully recycled into the simulation domain as neutrals at all surfaces, except for the cold ones of the cryo pump (see the rhombus-shaped structure in figure 1) where a

total recycling coefficient of 0.9 was assumed. This value corresponds to a pumping speed of about $50 \text{ m}^3 \text{ s}^{-1}$, for which the pump is designed. The fraction of fast and thermal particle reflection as well as the energy reflection coefficient are calculated by the TRIM and SDTrimSP database reflection models included in EIRENE [16]. N_2 gas is puffed into the PFR region (red arrow in figure 1) at different rates $\Phi_{N_2, \text{PFR}}$. There are more choices for the gas puff location (blue arrows in figure 1), however, in this paper we focus on the effect of the configuration. A short discussion of the role of the puffing location can nevertheless be found at the end of section 3, while a systematic investigation of the effect of the puffing location is foreseen for the near future.

3. Results

In simulations analyzed in the following, the input power and D^+ density at the innermost boundary are set to $P_{\text{in,core}} = 5 \text{ MW}$ and $n_{D^+, \text{core}} = 2 \times 10^{19} \text{ m}^{-3}$, respectively. Spatially and temporally constant diffusivity coefficients in the SOL are chosen as $D_{\perp} = 0.2 \text{ m}^2 \text{ s}^{-1}$ and $\chi_{\perp, e} = \chi_{\perp, i} = 0.6 \text{ m}^2 \text{ s}^{-1}$ in both SN and LFS SF^- configurations. Although a precise fit to experimentally measured profiles might require different and spatio-temporally varying transport coefficients, here we are interested in studying the effect of the geometry alone, while keeping the assumptions on the transport simple. Both configurations nevertheless have similar power fall-off lengths $\lambda_q = 2.9 \text{ mm}$ upstream, that are typical in AUG [17].

The transport coefficients are also similar to those used in the SOLPS simulations for ITER ($D_{\perp} = 0.3 \text{ m}^2 \text{ s}^{-1}$ and $\chi_{\perp,e} = \chi_{\perp,i} = 1.0 \text{ m}^2 \text{ s}^{-1}$) [18]. Figure 3 shows the poloidal cross sections of electron density, electron temperature and radiation power density computed by SOLPS for the SN (figures 3(a)–(c)) and the LFS SF[−] (figures 3(d)–(f)) configurations with the same nitrogen molecular seeding rates of $6.55 \times 10^{20} \text{ s}^{-1}$, corresponding to 9.17×10^{21} electrons per second. This magnitude is comparable with the typical experimental value for detached AUG lower SN discharges [19, 20]. Compared to the SN case, a high density and low temperature region expanding from OT₁ to the primary and secondary X-points can be seen in the LFS SF[−] case. The low temperature (<1 eV) at OT₁ (detailed target temperature profiles can be found in figure 6(d)) indicates that it is already in a detached state, while the outer target of the SN configuration is still in a high recycling regime. Meanwhile, the LFS SF[−] case shows a higher volumetric recombination rate and radiative fraction. These two processes are considered to play the most important roles in the reduction of the power and particle fluxes to a detached divertor target [21]. The total volumetric recombination rate in the LFS SF[−] case is $7.6 \times 10^{21} \text{ s}^{-1}$ (24% of the total ion flux to OT₁ and OT₂), while the value in the SN case is only $4.9 \times 10^{20} \text{ s}^{-1}$ (1% of the ion flux to the OT). Furthermore, a region of enhanced radiation can be seen in figure 3(f) between the primary and secondary X-points where the poloidal magnetic field is very weak. This large zone of weak poloidal field leads to an increased connection length and larger volume δV between two nearby flux surfaces separated by a given normalized poloidal flux $\delta \Psi_N$, which was predicted to be one of the benefits of the SF configuration [2]. As in [19], where AUG nitrogen seeding experiments were analyzed, we here define the radiation volume of nitrogen as the volume where the electron temperature is between 5 and 15 eV. In the simulation region, the radiation volume in the LFS SF[−] case is 39% larger than that in the SN case. The radiative fraction ($P_{\text{rad}}/P_{\text{in,core}}$) in the LFS SF[−] case reaches 86%, while in the SN case it is 79%. The radiation region between the X-points and the higher radiative fraction were also found in the simulations with EMC3-EIRENE in TCV [22]. In addition, a slightly (about 7%) lower nitrogen impurity concentration at the separatrix has been found in the LFS SF[−] case, indicating a lower impurity concentration in the core plasma in this configuration. More accurate quantitative predictions of the radiation in the confinement region are currently not available since these would require a neo-classical treatment of the impurities inside the separatrix [23].

In order to investigate the effect of the radiative power fraction on the target heat load, we here compare a low nitrogen seeding case (case A, $\Phi_{\text{N}_2} = 2.66 \times 10^{21} \text{ electrons s}^{-1}$) with the above mentioned high seeding case (case B, $\Phi_{\text{N}_2} = 9.17 \times 10^{21} \text{ electrons s}^{-1}$). The parallel heat fluxes to the targets for these two cases are shown in figures 4(a) and (b), respectively. Using the fitting function in [17], we obtained $\lambda_q = 3.0 \text{ mm}$, $S = 0.5 \text{ mm}$ and $q_{\parallel,\text{max,SN}} = 330 \text{ MW m}^{-2}$ for the SN outer target profile in case A, and $\lambda_q = 3.0 \text{ mm}$, $S = 1.6 \text{ mm}$ and $q_{\parallel,\text{max,SN}} = 59 \text{ MW m}^{-2}$ in case B. In contrast to [17], λ_q and

S are mapped here to the outboard mid-plane. When generalizing this formula to the LFS SF[−] configuration with equal maximum parallel heat load $q_{\parallel,\text{max,SF}}$ at OT₁ and OT₂, one finds a reduction of this maximum by a factor $q_{\parallel,\text{max,SF}}/q_{\parallel,\text{max,SN}} \approx (1 + 2.5\delta)/(1 + 5.0\delta)$ (taken from the fit formula, equation (8) in [3]), where $\delta = S/\lambda_q$, with respect to the maximum in the SN configuration. That means that by the effect of SOL splitting independently, $q_{\parallel,\text{max,SF}}$ would be about 255 and 38 MW m^{-2} for case A and B, respectively. The values found in the simulation are by 20% (case A) and 66% (case B) lower. This indicates that, apart from the SOL splitting effect, radiation contributes substantially to the power dissipation in the LFS SF[−] case. Note that the power distribution between OT₁ and OT₂ depend on the choice of transport coefficients D_{\perp} and χ_{\perp} . However, if these were different in the experiment, a different r_{u,x_2} can be chosen by varying the currents in the in-vessel coils in order to achieve an equal power repartition at least if the control system is accurate and fast enough to manage this. In addition to that the simulation showed that a moderate change of the transport coefficients would not change the main conclusion of this paper. A more detailed parameter scan is foreseen for a future publication.

It is also interesting to observe that the power flux to the IT in the LFS SF[−] configuration is also substantially smaller compared to that in the SN configuration, although the OMP to IT connection length is only marginally larger in the LFS SF[−] case (shown in figure 5). This is because the inner leg in case A is very close to the detachment threshold as confirmed by a control simulation in the SN configuration with slightly larger nitrogen puff.

The upstream radial profiles of electron density, ion and electron temperature as well as total pressure in the SN and LFS SF[−] configurations for case B are shown in figure 6. The total pressure and electron temperature profiles at the outer target are also shown in figures 6(c) and (d) with solid lines. The upstream density, electron and ion temperatures and consequently also the upstream pressure (figure 6(c), dotted lines) are very similar for the two configurations, whereas the total pressure downstream (figure 6(c), solid lines) is quite different. While basically no pressure loss is found for the SN case, the LFS SF[−] configuration shows a substantial (about 80%) pressure drop with respect to the upstream profile, indicating a significant momentum loss as expected for detached conditions. The low temperature at OT₁ shown in figure 6(d) is also characteristic for a detached divertor.

Besides puffing N₂ into the PFR region (red arrows in figures 1(a) and (b)), the same amount of nitrogen can also be puffed into the R2 or FARSOL regions (blue arrows in figure 1(b)). Differences in the radiation distribution as well as the power partition between OT₁ and OT₂ have been observed in these cases, but this will be investigated in a future publication. In this future study the puff location will be optimized according to the criterion to achieve the highest power dissipation in the divertor with the lowest separatrix impurity density. The freedom to inject N₂ directly into the region around the secondary X-point (instead of into the PFR

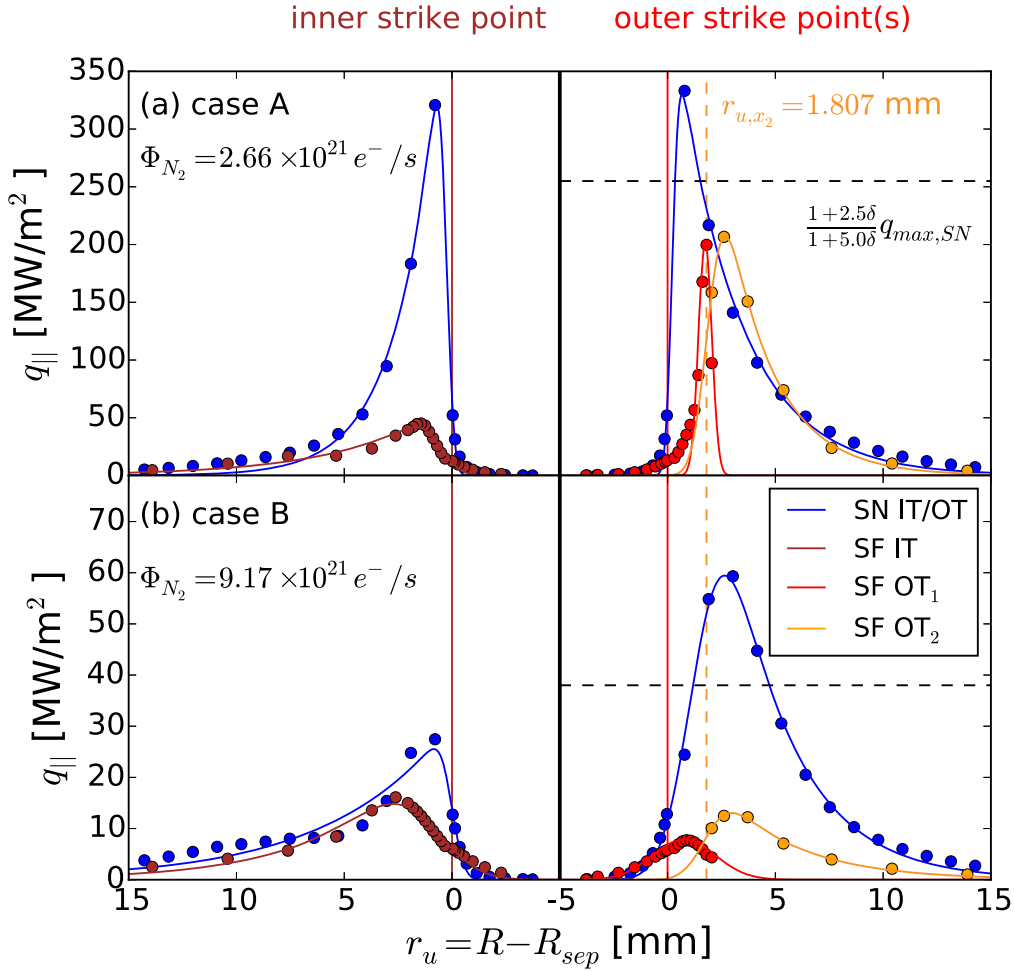


Figure 4. Parallel heat flux around the inner (left) and outer (right) strike points comparing the SN (blue) and LFS SF⁻ (reddish colors) configurations. The upper row shows the low nitrogen seeding case A ($\Phi_{N_2} = 2.66 \times 10^{21}$ electrons s⁻¹), where the outer target profiles are attached. For the high seeding case B ($\Phi_{N_2} = 9.17 \times 10^{21}$ electrons s⁻¹) the OT₁ of the LFS SF⁻ case is detached, while the outer target of the SN configuration is still in a high recycling regime. The maximum $q_{||}$ expected from a simple SOL splitting model [3] is indicated by the dashed black horizontal line. Due to other power dissipation processes the maximum in the simulation is significantly below this value.

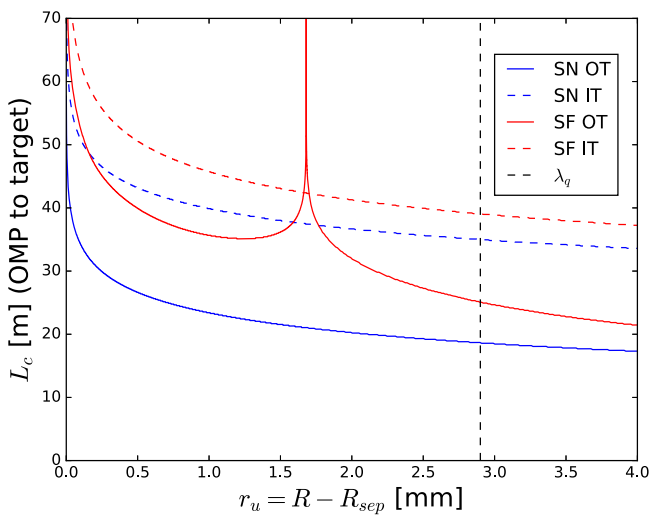


Figure 5. Outboard mid-plane to inner (dashed lines) and outer (solid lines) target connection length L_c for the LFS SF⁻ (red) and SN (blue) configurations. The vertical dashed line indicates the power decay length λ_q .

region) might facilitate the fulfillment of this criterion and might be one of the advantages of this configuration.

4. Summary and outlook

For the first time, SOLPS has been successfully applied for simulating a LFS SF⁻ configuration as it is planned for the upper divertor in AUG. This was possible by meeting several constraints concerning the resolution of the physical grid, that needs to be represented by a block-shaped computational grid. With constant transport coefficients $D = 0.2$ m² s⁻¹ and $\chi = 0.6$ m² s⁻¹, 5 MW input power and sufficient nitrogen seeding, stably converged solutions with radiative fractions up to 86% were obtained. Compared to a SN reference case with the same external simulation parameters as well as similar upstream profiles and separatrix impurity concentrations, the LFS SF⁻ configuration shows a 9% higher radiative fraction and a substantially higher volumetric recombination rate, which lead to an earlier detachment accompanied by a significant pressure loss in

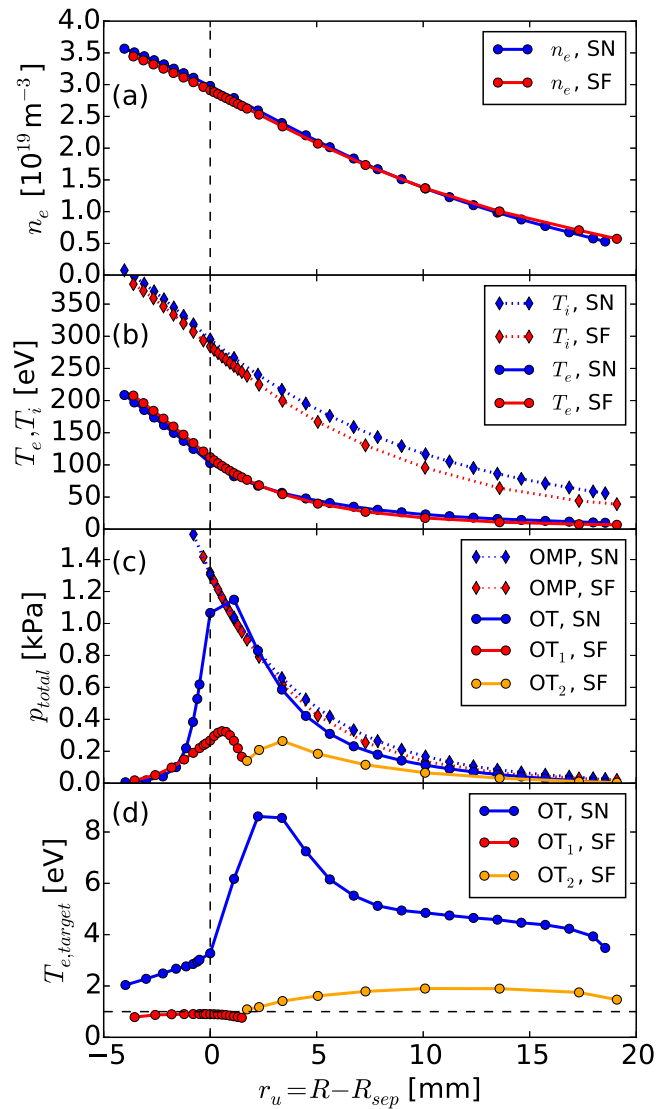


Figure 6. Outboard mid-plane (OMP) electron density (a) and electron and ion temperature (b) as a function of the OMP separatrix distance for the high nitrogen seeding case B. Plot (c) shows the upstream (dotted lines) total pressure compared to that at the target (solid lines). Plot (d) shows the target electron temperature profiles. The SN case is shown in blue and the LFS SF⁻ in reddish colors. A substantial (about 80%) pressure drop along the field line and a temperature profile lower than 1 eV at OT₁ are found in the LFS SF⁻ case, which indicates a significant degree of detachment.

the SOL, low target temperatures and a substantially reduced target heat load. It was shown that this effect is significantly stronger than expected from a simple SOL splitting model and is likely caused by enhanced radiation. As expected from previous EMC3-EIRENE simulations [22] this effect becomes stronger with higher radiative fraction. A more detailed parameter study with experimentally validated parameters to test the robustness

and universality of these results is foreseen for the near future. In addition to this the N₂ gas puff location is planned to be optimized by SOLPS simulations and the role of the different atomic and molecular processes will be studied. Preliminary runs with partly activated drifts were carried out, but further efforts need to be made to improve the convergence behavior. These also remain as future work.

Acknowledgments

This work has been carried out within the framework of the EUROfusion Consortium and has received funding from the Euratom research and training programme 2014–2018 under grant agreement No 633053. The views and opinions expressed herein do not necessarily reflect those of the European Commission.

ORCID iDs

O Pan  <https://orcid.org/0000-0003-3827-0674>

References

- [1] Kotschenreuther M *et al* 2007 *Phys. Plasmas* **14** 072502
- [2] Ryutov D *et al* 2012 *Plasma Phys. Control. Fusion* **54** 124050
- [3] Lunt T *et al* 2017 *Nucl. Mater. Energy* **12** 1037–42
- [4] Feng Y *et al* 2004 *Contrib. Plasma Phys.* **44** 57–69
- [5] Lunt T *et al* 2014 *Plasma Phys. Control. Fusion* **56** 035009
- [6] Lunt T *et al* 2015 *J. Nucl. Mater.* **463** 744–7
- [7] Potzel S *et al* 2015 *Nucl. Fusion* **54** 013001
- [8] Reimold F *et al* 2017 *Nucl. Mater. Energy* **12** 193–9
- [9] Meier E T *et al* 2015 *J. Nucl. Mater.* **463** 1200
- [10] Meier E T *et al* 2015 *Nucl. Fusion* **55** 086002
- [11] Mao R *et al* 2018 *Contrib. Plasma Phys.* (<https://doi.org/10.1002/ctpp.201700182>)
- [12] Schneider R *et al* 2006 *Contrib. Plasma Phys.* **46** 3–191
- [13] Braams B J 1992 A multi-fluid code for simulation of the edge plasma in tokamaks *Report on NET Contract 142/83-11/FU-NL/NET Princeton, USA*
- [14] Reiter D *et al* 2005 *Fusion Sci. Technol.* **47** 172–86
- [15] Kotov V *et al* 2008 *Plasma Phys. Control. Fusion* **50** 105012
- [16] Eckstein W 2009 Reflection (backscattering) *IPP Report 17/12 Max-Planck-Institut für Plasmaphysik* (http://pubman.mpg.de/pubman/item/escidoc:2141005/component/escidoc:2141004/IPP_report_17_12_Eckstein.pdf)
- [17] Eich T *et al* 2011 *Phys. Rev. Lett.* **107** 215001
- [18] Kukushkin A S *et al* 2003 *Nucl. Fusion* **43** 716
- [19] Kallenbach A *et al* 2013 *Plasma Phys. Control. Fusion* **55** 124041
- [20] Reimold F *et al* 2015 *Nucl. Fusion* **55** 033004
- [21] Krasheninnikov S I *et al* 2017 *J. Plasma Phys.* **83** 155830501
- [22] Lunt T *et al* 2016 *Plasma Phys. Control. Fusion* **58** 045027
- [23] Pütterich T *et al* 2011 *J. Nucl. Mater.* **451.1** S334–9